

Updated Global Analysis of the Atmospheric Neutrino Data in terms of neutrino oscillations

N. Fornengo^{a,b *}, M. C. Gonzalez-Garcia^{a §}, and J. W. F. Valle^{a †}

^a *Instituto de Física Corpuscular - C.S.I.C.*

Departamento de Física Teòrica, Universitat de València

Edificio Institutos de Paterna, Apt 2085, 46071 Valncia, Spain

^b *Dipartimento di Fisica Teorica, Università di Torino*

and INFN, Sez. di Torino, Via P. Giuria 1, I-10125 Torino, Italy

Abstract

A global analysis of all the available atmospheric neutrino data is presented in terms of neutrino oscillations in the $\nu_\mu \rightarrow \nu_\tau$ and $\nu_\mu \rightarrow \nu_s$ channels, where ν_s denotes a sterile neutrino. We perform our analysis of the contained events data as well as the upward-going neutrino-induced muon fluxes. In addition to the previous data samples of Frejus, Nusex, IMB and Kamioka experiments, we include the full data set of the 52 kton-yr of Super-Kamiokande, the recent 4.6 kton-yr contained events of Soudan2 and the results on upgoing muons from the MACRO and Baksan detectors. From the statistical analysis it emerges that the $\nu_\mu \rightarrow \nu_\tau$ channel provides the best agreement with the combined data, with a best fit point of $\sin^2(2\theta) = 0.99$ and $\Delta m^2 = 3.0 \times 10^{-3}$ eV². Although somehow disfavoured, the $\nu_\mu \rightarrow \nu_s$ channels cannot be ruled out on the basis of the global fit to the full set of observables.

Typeset using REVTeX

*E-mail: fornengo@flamenco.ific.uv.es

§E-mail: concha@flamenco.ific.uv.es

†E-mail: valle@flamenco.ific.uv.es

I. INTRODUCTION

Together with the solar neutrino problem [1] the atmospheric neutrino anomaly constitutes the second evidence for physics beyond the Standard Model. Indeed a large number of observations [2–12] have been performed concerning electron- and muon-neutrino fluxes produced by hadronic showers initiated by cosmic-ray interactions in the upper atmosphere. Apart from the first iron-calorimeter detectors [2,3], all experiments, which also entail different detection techniques, have steadily reported a deficit of the collected number of events with respect to the theoretical expectations [13,14]. Although the knowledge of the fluxes of atmospheric neutrinos is affected by uncertainties which range from about 20% to 30%, the expected ratio $R(\mu/e)$ of the muon neutrino ($\nu_\mu + \bar{\nu}_\mu$) over the electron neutrino flux ($\nu_e + \bar{\nu}_e$) is known with much better confidence, since the uncertainties associated with the absolute fluxes largely cancel out. It is fair to ascribe an overall uncertainty less than about 5% to the calculated $R(\mu/e)$ ratio. Since this ratio is measured to be substantially smaller than the expectations, one faces an anomaly which only seems possible to account for in terms of non-standard neutrino properties.

Super-Kamiokande high statistics observations [8,9] indicate that the deficit in the total ratio $R(\mu/e)$ is due to the neutrinos arriving in the detector at large zenith angles. They also show that the e -like events do not present any compelling evidence of a zenith-angle dependent suppression, while the μ -like event rates are substantially suppressed at large angles. Different explanations to these features have been proposed and discussed in the literature [15,16]. The simplest and most direct possibility is represented by the oscillation of muon neutrinos ν_μ into either a ν_τ or a sterile neutrino ν_s [17–19]. The oscillation hypothesis provides a very good explanation for this smaller-than-expected ratio, which is also simple and well-motivated theoretically.

In this paper we present our updated analysis of all the available data on atmospheric neutrinos in terms of neutrino oscillation. We include in the analysis all the existing experimental results obtained so far. In addition to the previous data samples of Frejus [2], Nussex [3], IMB [4] and Kamioka [7] experiments, we also consider the recent Soudan2 [6] data which refers to an exposure of 4.6 kton-yr, the full data set of the 52 kton-yr of Super-Kamiokande [10], including both contained events and upgoing muon data, and finally the results on upgoing muons reported from the MACRO [11] and Baksan [12] experiments. We critically discuss the analysis of the various individual data sets. Moreover we consider the combined information that can be derived from all the experimental evidences so-far obtained. We hope this will contribute to a more complete understanding of the atmospheric neutrino anomaly in the framework of a global analysis based on a self-consistent theoretical calculation of the event rates. This has the advantage of calibrating all relevant elements in the analysis, such as theoretical atmospheric neutrino fluxes, in a consistent way. This allows different experiments to be compared in a meaningful way. A new element which we now add to our previous investigations [17] is the inclusion of the upgoing muon data and the corresponding theoretical flux determinations [10–12]. We anticipate that from the statistical analysis the $\nu_\mu \rightarrow \nu_\tau$ emerges as the oscillation channel which provides the best agreement with the combined data. The $\nu_\mu \rightarrow \nu_s$ channels, although slightly disfavoured, cannot be statistically ruled out on the basis of the global fit to the full set of observables.

The outline of the paper is the following: in Sect. II we briefly recall the theoretical calculation of the event rates for contained events and upgoing muon fluxes, as well as the calculation of the oscillation probabilities. Sect. III discusses the statistical approach of our

analysis and reports on the results of the fits. Sect. IV presents a discussion of the results and the conclusions. We include more details on the statistical analysis in an Appendix.

II. ATMOSPHERIC NEUTRINO INDUCED EVENTS IN UNDERGROUND DETECTORS

Atmospheric neutrinos can be detected in underground experiments by direct observation of their charged current interaction inside the detector. These are the so-called contained events, which can be further classified into fully contained events when the charged lepton (either electron or muon) produced by the neutrino interaction does not escape the detector, and partially contained muons when the muon, produced inside, leaves the detector. In the case of Kamiokande and Super-Kamiokande, the contained data sample is further divided into sub-GeV events with visible energy below 1.2 GeV and multi-GeV events when the lepton energy is above such cutoff. On the average, sub-GeV events arise from neutrinos of several hundreds of MeV while multi-GeV events are originated by neutrinos with energies of the order of several GeV.

Higher energy muon neutrinos and anti-neutrinos can also be detected indirectly by observing the muons produced by charged current interactions in the vicinity of the detector. These are the so called upgoing muons. Should the muon stop inside the detector, it will be classified as a “stopping” muon, while if the muon track crosses the full detector the event is classified as a “through-going” muon. Typically stopping muons arise from neutrinos of energies around ten GeV while through-going muons are originated by neutrinos with energies of the order of hundred GeV.

A. Contained events

At present, six underground experiments have collected data on contained events. Three of them, Kamiokande [7] IMB [4] and Super-Kamiokande [8] use water-Cerenkov detectors, while the other three, Fréjus [2], NUSEX [3] and Soudan2 [5,6] are iron calorimeter detectors.

For a given neutrino conversion mechanism, the expected number of μ -like and e -like contained events, N_α , $\alpha = \mu, e$ can be computed as:

$$N_\mu = N_{\mu\mu} + N_{e\mu}, \quad N_e = N_{ee} + N_{\mu e}, \quad (1)$$

where

$$N_{\alpha\beta} = n_t T \int \frac{d^2\Phi_\alpha}{dE_\nu d(\cos\theta_\nu)} \kappa_\alpha(h, \cos\theta_\nu, E_\nu) P_{\alpha\beta} \frac{d\sigma}{dE_\beta} \varepsilon(E_\beta) dE_\nu dE_\beta d(\cos\theta_\nu) dh \quad (2)$$

and $P_{\alpha\beta}$ is the conversion probability of $\nu_\alpha \rightarrow \nu_\beta$ for given values of E_ν , $\cos\theta_\nu$ and h , *i.e.*, $P_{\alpha\beta} \equiv P(\nu_\alpha \rightarrow \nu_\beta; E_\nu, \cos\theta_\nu, h)$. In the Standard Model (SM), the only non-zero elements are the diagonal ones, *i.e.* $P_{\alpha\alpha} = 1$ for all α . In Eq.(2) n_t denotes the number of targets, T is the experiment running time, E_ν is the neutrino energy and Φ_α is the flux of atmospheric neutrinos of type $\alpha = \mu, e$ for which we use the Bartol flux [13]; E_β is the final charged lepton energy and $\varepsilon(E_\beta)$ is the detection efficiency for such charged lepton; σ is the neutrino-nucleon interaction cross section, and θ_ν is the angle between the vertical direction and the incoming neutrinos ($\cos\theta_\nu=1$ corresponds to the down-coming neutrinos). In Eq. (2), h is the slant

distance from the production point to the sea level for α -type neutrinos with energy E_ν and zenith angle θ_ν . Finally, κ_α is the slant distance distribution, normalized to one [20]. For the angular distribution of events we integrate in the corresponding bins for $\cos\theta_\beta$ where θ_β is the angle of the detected lepton, taking into account the opening angle between the neutrino and the charged lepton directions as determined by the kinematics of the neutrino interaction. In average the angle between the directions of the final-state lepton and the incoming neutrino ranges from 70° at 200 MeV to 20° at 1.5 GeV.

The neutrino fluxes, in particular in the sub-GeV range, depend on the solar activity. In order to take this fact into account, we use in Eq. (2) a linear combination of atmospheric neutrino fluxes Φ_α^{max} and Φ_α^{min} which correspond to the most active Sun (solar maximum) and quiet Sun (solar minimum), respectively, with different weights which depend on the running period of each experiment [17]. Following Ref. [17] we explicitly verify in our present reanalysis the agreement of our predictions with the experimental Monte Carlo predictions, leading to a good confidence in the reliability of our results for contained events.

B. Upward Going Muons

Several experiments have obtained data on these neutrino induced muons. In our analysis we consider the results from three experiments: Super-Kamiokande [9], MACRO [11] and Baksan [12]. They present their upgoing muon data in the form of measured muon fluxes. We obtain the effective muon fluxes for both stopping and through-going muons by convoluting the survival ν_μ probabilities (calculated as in Sect. II.C) with the corresponding muon fluxes produced by the neutrino interactions with the Earth. We include the muon energy loss during propagation both in the rock and in the detector according to Refs. [21,22] and we take into account also the effective detector area for both types of events, stopping and through-going. Schematically

$$\Phi_\mu(\theta)_{S,T} = \frac{1}{A(L_{min}, \theta)} \int_{E_{\mu,min}}^{\infty} \frac{d\Phi_\mu(E_\mu, \cos\theta)}{dE_\mu d\cos\theta} A_{S,T}(E_\mu, \theta) dE_\mu, \quad (3)$$

where

$$\begin{aligned} \frac{d\Phi_\mu}{dE_\mu d\cos\theta} &= N_A \int_{E_\mu}^{\infty} dE_{\mu 0} \int_{E_{\mu 0}}^{\infty} dE_\nu \int_0^{\infty} dX \int_0^{\infty} dh \kappa_{\nu_\mu}(h, \cos\theta, E_\nu) \\ &\frac{d\Phi_{\nu_\mu}(E_\nu, \theta)}{dE_\nu d\cos\theta} P_{\mu\mu} \frac{d\sigma(E_\nu, E_{\mu 0})}{dE_{\mu 0}} F_{rock}(E_{\mu 0}, E_\mu, X) \end{aligned} \quad (4)$$

N_A is the Avogadro number, $E_{\mu 0}$ is the energy of the muon produced in the neutrino interaction and E_μ is the muon energy when entering the detector after traveling a distance X in the rock. $\cos\theta$ labels both the neutrino and the muon directions which to a very good approximation at the relevant energies are collinear. We denote by $F_{rock}(E_{\mu 0}, E_\mu, X)$ the function which characterizes the energy spectrum of the muons arriving the detector. Following standard practice [21,22] in our calculations we use the analytical approximation obtained by neglecting the fluctuations during muon propagation in the Earth. In this case the three quantities $E_{\mu 0}$, E_μ , and X are not independent:

$$\int_0^{\infty} F_{rock}(E_{\mu 0}, E_\mu, X) dX = \frac{1}{\langle dE_\mu(E_\mu)/dX \rangle}, \quad (5)$$

where $\langle d\mathcal{E}_\mu(E_\mu)/dX \rangle$ is the average muon energy loss due to ionization, bremsstrahlung, e^+e^- pair production and nuclear interactions in the rock according to Refs. [21,22]. Equivalently, the pathlength traveled by the muon inside the Super-Kamiokande detector is given by the muon range function in water

$$L(E_\mu) = \int_0^{E_\mu} \frac{1}{\langle d\mathcal{E}_\mu(E'_\mu)/dX \rangle} dE'_\mu. \quad (6)$$

In Eq.(3) $A(L_{min}, \theta) = A_S(E_\mu, \theta) + A_T(E_\mu, \theta)$ is the projected detector area for internal path-lengths longer than L_{min} which for Super-Kamiokande is $L_{min} = 7$ m. Here A_S and A_T are the corresponding effective areas for stopping and through-going muon trajectories. For Super-Kamiokande we compute these effective areas using the simple geometrical picture given in Ref. [23]. For a given angle, the threshold energy cut for Super-Kamiokande muons is obtained by equating Eq.(6) to L_{min} , i.e. $L(E_\mu^{th}) = L_{min}$.

In contrast with Super-Kamiokande, Baksan and MACRO present their results as muon fluxes for $E_\mu > 1$ GeV, after correcting for detector acceptances. Therefore in this case we compute the expected fluxes as Eqs. (3) and (4) but without the inclusion of the effective areas.

We have explicitly verified the agreement of our predictions for upgoing muons with the experimental Monte Carlo predictions from Super-Kamiokande, Baksan and MACRO. The agreement can be observed by comparing our Standard Model predictions for the angular distributions in Fig. 6 with the corresponding distributions in Refs. [10] and [11]. We find an agreement to the 5% and 1% level, respectively.

C. Conversion Probabilities

For definiteness we assume a two-flavour scenario. The oscillation probabilities are obtained by solving the Schrödinger evolution equation of the $\nu_\mu - \nu_X$ system in the Earth-matter background (in our case, $X = \tau$ or s). For *neutrinos* this equation reads:

$$i \frac{d}{dt} \begin{pmatrix} \nu_\mu \\ \nu_X \end{pmatrix} = \begin{pmatrix} H_\mu & H_{\mu X} \\ H_{\mu X} & H_X \end{pmatrix} \begin{pmatrix} \nu_\mu \\ \nu_X \end{pmatrix} \quad (7)$$

where

$$H_\mu = V_\mu + \frac{\Delta m^2}{4E_\nu} \cos 2\theta, \quad (8)$$

$$H_X = V_X - \frac{\Delta m^2}{4E_\nu} \cos 2\theta, \quad (9)$$

$$H_{\mu X} = -\frac{\Delta m^2}{4E_\nu} \sin 2\theta, \quad (10)$$

with the following definition of the neutrino potentials in matter

$$V_\mu = V_\tau = \frac{\sqrt{2}G_F\rho}{M} \left(-\frac{1}{2}Y_n\right), \quad (11)$$

$$V_s = 0. \quad (12)$$

Here G_F is the Fermi constant, ρ is the matter density in the Earth, M is the nucleon mass, and Y_n is the neutron fraction. For anti-neutrinos the signs of potentials V_X should be reversed. In the previous Eqs., θ is the mixing angle between the two mass eigenstate neutrinos of masses m_1 and m_2 . We define $\Delta m^2 = m_2^2 - m_1^2$ in such a way that if $\Delta m^2 > 0$ ($\Delta m^2 < 0$) the neutrino with largest muon-like component is heavier (lighter) than the one with largest X -like component.

Since for the $\nu_\mu \rightarrow \nu_\tau$ case there is no matter effect, the solution of Eq.(7) is straightforward and the probability takes the well-known vacuum form

$$P_{\mu\mu} = 1 - \sin^2(2\theta) \sin^2\left(\frac{\Delta m^2 L}{2E_\nu}\right). \quad (13)$$

where L is the path-length traveled by neutrinos of energy E_ν .

In the case of $\nu_\mu \rightarrow \nu_s$, the presence of the matter potentials requires a numerical solution of the evolution equations in order to obtain the oscillation probabilities $P_{\alpha\beta}$, which are different for neutrinos and anti-neutrinos because of the reversal of sign of the V_X 's. In our calculations, for the matter density profile of the Earth we have used the approximate analytic parametrization given in Ref. [24] of the PREM model of the Earth [25]. Notice that for the $\nu_\mu \rightarrow \nu_s$ case, there are two possibilities depending on the sign of Δm^2 . For $\Delta m^2 > 0$ the matter effects enhance *neutrino* oscillations while depress *anti-neutrino* oscillations, whereas for the other sign ($\Delta m^2 < 0$) the opposite holds.

Finally, we have not considered oscillations of ν_μ 's into electron neutrinos. This possibility is nowadays ruled out since $\nu_\mu \rightarrow \nu_e$ oscillations cannot describe the measured angular dependence of muon-like contained events [17]. Moreover the most favoured range of masses and mixings for this channel has already been excluded by the negative results from the CHOOZ reactor experiment [26].

III. ATMOSPHERIC NEUTRINO DATA FITS

In this Section, we describe the fitting procedure we employ in order to determine the atmospheric neutrino parameters $\sin^2(2\theta)$ and Δm^2 for the two conversion channels of interest and we present our results.

A. Statistical analysis

We first notice that we rely on the separate use of the event numbers (not of their ratios), paying attention to the correlations between the sources of errors in the muon and electron predictions as well as the correlations among the errors of the different energy data samples.

A detailed description of the steps required in order to determine the allowed regions of oscillation parameters was given in Ref. [17]. Following Refs. [17,27,28], we define a χ^2 -function as

$$\chi^2 \equiv \sum_{I,J} (N_I^{DATA} - N_I^{TH}) \cdot (\sigma_{DATA}^2 + \sigma_{TH}^2)^{-1}_{IJ} \cdot (N_J^{DATA} - N_J^{TH}), \quad (14)$$

where I and J stand for any combination of experimental data sets and event-types considered, *i.e.*, $I = (A, \alpha)$ and $J = (B, \beta)$. The latin indexes A, B stand for the different

experiments or different data samples in a given experiment. The greek indexes denote electron-type or muon-type events, *i.e.*, $\alpha, \beta = e, \mu$. In Eq. (14), N_I^{TH} stands for the predicted number of events (or for the predicted value of the flux, in the case of upgoing muons) calculated as discussed in the previous Section, whereas N_I^{DATA} is the corresponding experimental measurement. In Eq. (14), σ_{DATA}^2 and σ_{TH}^2 are the error matrices containing the experimental and theoretical errors, respectively. They can be written as

$$\sigma_{IJ}^2 \equiv \sigma_\alpha(A) \rho_{\alpha\beta}(A, B) \sigma_\beta(B), \quad (15)$$

where $\rho_{\alpha\beta}(A, B)$ is the correlation matrix containing all the correlations between the α -like events in the A -type experiment and β -like events in B -type experiment, whereas $\sigma_\alpha(A)$ and $\sigma_\beta(B)$ are the errors for the number of α and β -like events in A and B experiments, respectively. The dimensionality of the error matrix varies depending on the combination of experiments included in the analysis.

We have computed the correlation matrix $\rho_{\alpha\beta}(A, B)$ as described in Ref. [27]. In the case of contained events, a detailed discussion of the errors and correlations used in our analysis can be found in Ref. [17], which, for the sake of clarity and completeness, we summarize in the Appendix. In the same Appendix, we include the discussion of the errors and correlations employed for the upgoing muon data analysis.

With all the definitions discussed above, we can calculate the χ^2 in Eq. (14) as a function of the neutrino parameters. By minimization of the χ^2 with respect to $\sin^2(2\theta)$ and Δm^2 , we determine our best fit results, while the allowed regions are determined by the following conditions: $\chi^2 \equiv \chi_{\min}^2 + 4.61 (6.1) [9.21]$ for a confidence level (CL) of 90 (95) [99] %, respectively.

The data sets employed in the statistical analysis are the following: (i) Frejus [2], Nusex [3], IMB [4] and Soudan2 [6] data sets, which refer to low-energy, contained events. For each experiment, the total rate for e -like and for μ -like events is reported. We jointly analyze these data (and hereafter we collectively denote them as FISN); (ii) e -like and μ -like Kamiokande data [7], including the sub-GeV event rate and a 5-bin zenith-angle distribution for the multi-GeV data; (iii) Super-Kamiokande data [10], again comprising e -like and μ -like contained events, arranged into sub-GeV and multi-GeV samples, each of which given as a 5-bin zenith-angle distribution; and the up-going data including the stopping muon flux (5 bins in zenith-angle) and the through-going muon flux (10 angular bins); (iv) MACRO [11] and Baksan [12] upgoing muons samples, each one with 10 angular bins.

In the discussion of our results, along with presenting the results of the separate analyses of the single data sets, we analyze various possible combinations of data samples in order to develop an understanding of the relevance of the different sets of data, which, we recall, refer to events characterized by different properties. For instance, contained events are produced by neutrinos of relatively low energies (below a few GeV), while the upgoing muon fluxes are originated by neutrinos whose energies cover a much wider range, from a few GeV to hundreds of GeV. This feature, combined also with the angular distributions, allows one to test the energy dependence of the oscillation probabilities in the different channels.

B. Results of the analysis

As a first result of our analysis, we show the (in)consistency of the data with the Standard Model hypothesis. The first column of Table I reports the values of the χ^2 function in

the absence of new physics, as obtained with our prescriptions and calculated for different combinations of atmospheric data sets. We notice that all the data sets clearly indicate deviation from the standard model. The global analysis, which refers to the full combination of all data sets, gives a value of $\chi_{SM,global}^2 = 214/(75 \text{ d.o.f.})$ corresponding to a CL of 3×10^{-15} . This indicates that the Standard Model can be safely ruled out. Instead, the χ^2 for the global analysis decreases to $\chi_{min}^2 = 74/(73 \text{ d.o.f.})$ (45 % CL) when assuming the $\nu_\mu \rightarrow \nu_\tau$ oscillation hypothesis.

Table I reports the minimum values of χ^2 and the resulting best fit points for the various oscillation channels and data sets considered. The corresponding allowed regions for the oscillation parameters at 90, 95 and 99 % CL are depicted in Figs. 1, 3, 4, 5 and 7. The zenith-angle distributions referring to the Super–Kamiokande data and to the upgoing muon measurements of MACRO and Baksan are plotted in Figs. 2, 6 and 8. Note that no uncertainties are shown in the plots for the theoretical predictions, while experimental data errors are explicitly displayed. We now turn to the discussion of the main results.

1. Contained Events

The allowed regions for contained events are displayed in Figs. 1 and 3. In all figures the best fit points are marked with a star and can be read from Table I together with the corresponding value of the χ_{min}^2 for each case.

In the first column of Fig. 1 we show the results for the combination of the “unbinned” FISN data, *i.e.* the total rates from the Frejus, IMB, Nusex and Soudan experiments. Since no angular information is present in this case, no lower limit on the oscillation length can be derived and the regions extend to arbitrary large mass differences. We notice, from Table I, that the best fit results, although definitely improved with respect to the SM case, do not show, for each oscillation channel, a CL better than 4%. We remind that the FISN data sample contains the Frejus and Nusex data, which are by themselves compatible with the SM. This fact plays a role in maintaining a relatively high χ^2 even in the oscillation cases.

The second column of Fig. 1 corresponds to the combination of contained sub-GeV (unbinned) and multi-GeV (including the angular dependence) data from the Kamiokande experiment. In this case, the angular distribution of the multi-GeV events plays an important role in determining an upper limit for Δm^2 , for a given value of the mixing angle. The region which is obtained overlaps with the previous one from the FISN data sample, and indicates a preference for values of $\Delta m^2 \gtrsim 10^{-3}$ for all the oscillation channels. For the Kamiokande data, the agreement with the oscillation hypothesis is at the level of $\sim 70\%$ CL.

Finally, in the third column of Fig. 1 we plot the allowed regions for the combination of the angular distributions of the sub-GeV and multi-GeV 52 kton-yr Super–Kamiokande data. The best fit for the $\nu_\mu \rightarrow \nu_\tau$ hypothesis has a very high confidence level: $\chi_{min}^2 = 8.9/(18 \text{ d.o.f.})$, which translates into 96% CL, substantially improved with respect to the Kamiokande data sets. In the case of oscillation to sterile neutrinos, the CL is 79%, slightly higher than for the Kamiokande data alone. The angular distributions of the Super–Kamiokande sub-GeV and multi-GeV μ -like events are shown in Fig. 2. We also show in the figure the e -like distributions to illustrate that they do not show any evidence of deviation from the standard model prediction. The agreement of the e -like distributions with the expectations from the standard model has become more tight as the Super–Kamiokande collaboration has been increasing their data sample. This has translated into an overall improvement of the

CL for the oscillation hypothesis into channels not involving electron neutrinos. Conversely solutions involving oscillations into electron neutrinos have become more disfavoured [28,31].

From Fig. 2 one sees that there is a strong evidence of a depletion in the event rates with respect to the SM expectation. We notice that the zenith-angle distributions obtained with the best-fit neutrino parameters are able to reproduce the data to a high level of agreement.

From Fig. 1, one can notice that in all the $\nu_\mu \rightarrow \nu_s$ channels where matter effects play a role, the range of acceptable Δm^2 is slightly shifted towards larger values, when compared with the $\nu_\mu \rightarrow \nu_\tau$ case. This follows from looking at the relation between mixing *in vacuo* and in matter. In fact, away from the resonance region, independently of the sign of the matter potential, there is a suppression of the mixing inside the Earth. As a result, there is a lower cut in the allowed Δm^2 value, and this lies higher than what is obtained in the case of the $\nu_\mu \rightarrow \nu_\tau$ channel. Also, for the $\nu_\mu \rightarrow \nu_s$ case with $\Delta m^2 > 0$ the matter effects enhance *neutrino* oscillations while depress *anti-neutrino* oscillations. Since atmospheric fluxes are dominantly neutrinos, smaller mixing angle values can lead to the same ν_μ suppression and the region extends to smaller mixing angles in the Δm^2 region where the matter effects are important for the relevant neutrino energies. The opposite holds for $\Delta m^2 < 0$. In this case the matter effects depress *neutrino* oscillations, and therefore larger mixing angles are needed to account for the observed deficit. As a consequence, the allowed regions become smaller (in angle) for this channel.

When comparing our results with the corresponding analysis presented by the Super-Kamiokande Collaboration on their data sets, we find good agreement on the allowed parameters although in general our regions are slightly larger. We also find that, for the $\nu_\mu \rightarrow \nu_\tau$ channel, the allowed regions for the contained events are shifted towards slightly lower Δm^2 values with respect to Super-Kamiokande analysis. We have traced this difference back to the sub-GeV sample and to our use of different neutrino fluxes. Notice that sub-GeV events are most sensitive to details in the neutrino fluxes from the different calculations, such as the modeling of the geo-magnetic cut-off [29]. The expected angular distribution in the absence of oscillations from the Super-Kamiokande Monte-Carlo using Honda fluxes is slightly “flatter” than our calculations for the sub-GeV event distributions. We have verified that if we normalize our results to the Super-Kamiokande Monte-Carlo predictions, then the allowed region we obtain is shifted to slightly larger Δm^2 values in agreement with the Super-Kamiokande analysis.

Finally, the global analysis of the combination of all the above data sets is shown in the first column of Fig. 3 (notice a change of scale between this figure and Fig. 1). The allowed regions, as well as the best fit points, are clearly driven by the high statistics Super-Kamiokande data. The results show, as expected from the above discussion, that the $\nu_\mu \rightarrow \nu_\tau$ case prefers slightly lower values of Δm^2 (from a few 10^{-4} to a few 10^{-3} eV²) when compared to the $\nu_\mu \rightarrow \nu_s$ cases, where values in excess of 10^{-3} eV² are obtained. In all the cases, almost-maximal mixing is statistically preferred. Concerning the quality of the fits, as seen in Table I, in the full combination the $\nu_\mu \rightarrow \nu_\tau$ channel gives a slightly better fit ($\chi_{min}^2 = 37/38$) than $\nu_\mu \rightarrow \nu_s$ ($\chi_{min}^2 = 40/38$) although the difference is not statistically significant (51% CL versus 38% CL).

2. Upward Going Muons

Our results for the allowed regions for upgoing muon events are displayed in Figs. 4 for the Super-Kamiokande data on stopping and through-going muons and in Fig. 5 for the MACRO and Baksan experiments. The global analysis on all the data samples on upgoing muons is shown in the second column of Fig. 3.

From the analysis of Super-Kamiokande data on stopping muons we find that the χ^2 -function is substantially flat for Δm^2 values above 10^{-3} eV² and $\sin^2(2\theta) \gtrsim 0.5$ and therefore the allowed regions are open from above, also at 90 % CL. This is a consequence of the fact that the stopping muons data sample by its own is consistent with a global reduction of the neutrino flux with no specific angular dependence. This feature can be observed by comparing the angular distribution of the data points in the first panel of Fig. 6 and the corresponding prediction in the absence of oscillations. This behaviour is what is expected from oscillations with short oscillation lengths (high Δm^2).

In contrast, the through-going Super-Kamiokande muon sample indicates a somewhat angular-dependent suppression. The second panel of Fig. 6 shows that the reduction is clearly larger for vertically-coming muons than for those arriving from the horizon. As a consequence, the corresponding allowed regions turn out to be closed from above, *i.e.* for large Δm^2 . This is plotted in the second column of Fig. 4, whose comparison with the first column shows the general agreement between the stopping and through-going muons data samples. This is an interesting property in favour of the neutrino oscillation hypothesis, since, as noted before, stopping and through-going muon events originate from very different parent-neutrino energies.

Finally, the combination of both stopping and thru-going muon events in Super-Kamiokande is shown in the third column of Fig. 4. We find a very good agreement between our results and the corresponding ones given by the Super-Kamiokande Collaboration. The best fit points in ours and the Super-Kamiokande analyses are very similar, although also in this case our regions are slightly larger. From the angular distributions of Fig. (6), we can observe that due to matter effects the distribution for upgoing muons in the case of $\nu_\mu \rightarrow \nu_s$ are flatter than for $\nu_\mu \rightarrow \nu_\tau$ [30,23]. Since the data show a somehow steeper angular dependence, a better description in terms of $\nu_\mu \rightarrow \nu_\tau$ oscillations is found. From Table I, we see that the upward going muon fit in this channel is indeed better, although the statistical preference of this channel over the sterile case (45% CL for $\nu_\mu \rightarrow \nu_\tau$ as compared to about 30% CL for $\nu_\mu \rightarrow \nu_s$) is not overwhelming.

In the case of both MACRO and Baksan experiments we generally find a less significant statistical agreement between the data and the theoretical evaluations. Both data sets are clearly inconsistent with the SM predictions, as indicated by their high χ_{SM}^2 values in Table I: the CL are 7×10^{-4} for MACRO and 5×10^{-3} for Baksan. However, the quality of the fits does not strongly improve when interpreted in terms of neutrino oscillations. We find that the best agreement occurs for the oscillation in the $\nu_\mu \rightarrow \nu_\tau$ channel for the MACRO experiment. In this case we obtain a 5% CL and an allowed region in the parameter space, which is shown in the first panel of Fig. 5. This result is fully consistent with the analysis performed by the MACRO Collaboration on their data set [11]. We notice that, as can be seen from the angular distribution of Fig. 6, the flux in the fourth bin ($-0.7 < \cos \theta_Z < -0.6$) is at least $2\text{-}\sigma$ above the expectation in the presence of oscillations. When removing this point from the statistical analysis, the quality of the fit for the $\nu_\mu \rightarrow \nu_\tau$ oscillation channel improves to 19% CL, while affecting very little the allowed region. In contrast, for the sterile

cases, we encounter a very low statistical confidence (about 1% CL), even after removing the fourth bin data point. As a result the corresponding allowed oscillation parameter regions are not very meaningful, since the best fit point has a large χ_{\min}^2 value. For this reason we have not reproduced them here. We only comment that the χ^2 is very flat in the neutrino oscillation parameters, without a clear indication of a statistically preferred region. In the $\Delta m^2 > 0$ case, two almost degenerate minima are found, one for small and one for large mixing angle, as can be seen in Table I).

For Baksan we find no clear preference for the oscillation hypothesis with respect to the Standard Model case, although in the sterile channels the best fits with oscillation turn out to be slightly better than for the no-oscillation case. We reproduce in Fig. 5 the allowed region for the $\nu_\mu \rightarrow \nu_s$ ($\Delta m^2 > 0$) case, which is the one with lowest χ^2 . In the case of $\nu_\mu \rightarrow \nu_\tau$ and $\nu_\mu \rightarrow \nu_s$ ($\Delta m^2 < 0$), the allowed regions are very similar to the one depicted in Fig. 5. We wish to warn that, due to the low statistical significance of the best fit results, these regions should be taken only as indicative.

To conclude this Section, we show in the right column of Fig. 3 the result of our analysis for the combination of all the data on upgoing muons discussed above. In the case of $\nu_\mu \rightarrow \nu_\tau$, one notices that the Super-Kamiokande and MACRO results give consistent and similar allowed regions, while Baksan gives compatible but not strongly constraining results. As a consequence, the combined analysis gives a region which is intermediate to the Super-Kamiokande and MACRO ones. The best fits of the combined upgoing neutrino analysis have a low CL (around 1% for all the oscillation channels), a result which is mainly driven by the high χ_{\min}^2 values of MACRO and Baksan (we recall that Super-Kamiokande upgoing-muon data alone indicate a preference for neutrino oscillation at a level always better than 25%). However, the global analysis of the upgoing muons data disfavours the Standard Model at the 3×10^{-5} level.

3. Global Analysis

Let us now move to the discussion of the comparison and combination of contained events with upgoing muons fluxes. We observe from Fig. 3 that the allowed regions obtained from both types of analyses are fully consistent between themselves for all the oscillation channels. For the cases of $\nu_\mu \rightarrow \nu_s$ the allowed region for the contained events lies always inside the corresponding regions allowed by the upgoing muon analysis. For the $\nu_\mu \rightarrow \nu_\tau$ channel, we find that the region for contained events extends to lower values of Δm^2 , when compared to the region for upgoing muons.

In figure 7 we display the allowed regions after combining together contained and upward going muon data. In the first column we show the results when only including the Super-Kamiokande data. The second column shows the corresponding results when data from all experiments are included, while in the third column we show the allowed regions when only the results from experiments observing some evidence of neutrino oscillation are included. The general behaviour is that when including the results from all experiments the regions become slightly larger than those obtained from the analysis of the Super-Kamiokande data alone. On the other hand, as expected, the results become more restrictive when only the data from experiments observing some evidence for oscillations are included. In Table I we list the values of the best fit points for the various cases.

Our results from the combined analysis show that the channel $\nu_\mu \rightarrow \nu_\tau$ gives a better

fit to the data than oscillations into sterile neutrinos. The difference for the global analysis is $\chi_{min}^2 = 74/(73 \text{ d.o.f.})$ (45 % CL) for the active case versus $\chi_{min}^2 = 90/(73 \text{ d.o.f.})$ (8.5 % CL) for oscillations into sterile neutrinos with $\Delta m^2 < 0$ and $\chi_{min}^2 = 86/(73 \text{ d.o.f.})$ (14 % CL) for $\nu_\mu \rightarrow \nu_s$ with $\Delta m^2 > 0$. This difference in the quality of the description is still maintained when some of the negative-result experiments are excluded from the analysis (by “negative-result experiments” we mean experiments which, from our statistical analysis, do not give a clear evidence of neutrino oscillation, *i.e.* have relatively high χ_{min}^2 values). All of these features can be seen in Table I. When removing from the analysis the Frejus, Nusex and Baksan data points, we do not obtain an improvement for the sterile cases, while for the active case the CL is increased to 58 % ($\chi_{min}^2 = 58/(61 \text{ d.o.f.})$). When also MACRO is removed, we obtain higher CL also for the sterile cases, but the $\nu_\mu \rightarrow \nu_\tau$ hypothesis remains as the best option: $\chi_{min}^2 = 41/(51 \text{ d.o.f.})$ (84 % CL) for the active case, $\chi_{min}^2 = 51/(51 \text{ d.o.f.})$ (47 % CL) for $\nu_\mu \rightarrow \nu_s$ with $\Delta m^2 < 0$ and $\chi_{min}^2 = 50/(51 \text{ d.o.f.})$ (51 % CL) for $\nu_\mu \rightarrow \nu_s$ with $\Delta m^2 > 0$.

In conclusion, we find that the quality of the global description is better for the $\nu_\mu \rightarrow \nu_\tau$ channel although oscillations into $\nu_\mu \rightarrow \nu_s$ cannot be statistically ruled out on the basis of the global fit to the full set of observables. In Fig. 8 we show the zenith-angle distributions for the Super-Kamiokande data sets, calculated for the best-fit points obtained in the global analysis of the data, when only “positive results” experiments are considered. From the figure, we notice that the $\nu_\mu \rightarrow \nu_s$ cases have more difficulties in reproducing the distribution of the data points because for $\nu_\mu \rightarrow \nu_s$ the survival probability of muon-neutrinos has a less steep angular behaviour as compared with the $\nu_\mu \rightarrow \nu_\tau$ case due to the Earth matter effects present in the $\nu_\mu \rightarrow \nu_s$ channels.

IV. DISCUSSION

In this paper we have performed a global analysis of the atmospheric neutrino data in terms of neutrino oscillations. We have compared the relative statistical relevance of the active-active and active-sterile channels as potential explanations of the atmospheric neutrino anomaly. In the analysis we have included, for the contained events, the latest data from Super-Kamiokande, corresponding to 52 kton-yr, together with all other available atmospheric neutrino data in the sub-GeV and multi-GeV range. Specifically, we included the data sets of the Frejus, Nusex, IMB, Soudan2 and Kamiokande experiments. Our analysis also includes the results on neutrino induced upgoing muons from the Super-Kamiokande 52 kton-yr sample, from MACRO and from Baksan experiments. We have determined the best-fit neutrino oscillation parameters and the resulting allowed regions in $\sin^2(2\theta)$ and Δm^2 for $\nu_\mu \rightarrow \nu_X$ ($X = \tau, s$) channels. For oscillations into sterile neutrinos we have considered both positive and negative Δm^2 , since the two cases differ in the matter effect for neutrinos propagation in the Earth.

The results of the combined analysis indicate that the channel $\nu_\mu \rightarrow \nu_\tau$ gives a better fit to the data than oscillations into sterile neutrinos: $\chi_{min}^2 = 74/(73 \text{ d.o.f.})$ (45 % CL) for the active case versus $\chi_{min}^2 = 90/(73 \text{ d.o.f.})$ (8.5 % CL) for oscillations into sterile neutrinos with $\Delta m^2 < 0$ and $\chi_{min}^2 = 86/(73 \text{ d.o.f.})$ (14 % CL) for $\nu_\mu \rightarrow \nu_s$ with $\Delta m^2 > 0$. Since for some experiments we obtain large χ_{min}^2 values also for neutrino oscillations, values not clearly better than the analysis for the standard model case, we decided to perform additional analyses by removing these “negative-result experiments”. When excluding Frejus, Nusex

and Baksan data points, we do not obtain an improvement for the sterile cases, while for the active case the CL is increased to 58 % ($\chi_{min}^2 = 58/(61 \text{ d.o.f.})$). When also MACRO is removed, we obtain higher CL also for the sterile cases, but the $\nu_\mu \rightarrow \nu_\tau$ hypothesis remains as the best option: $\chi_{min}^2 = 41/(51 \text{ d.o.f.})$ (84 % CL) for the active case, $\chi_{min}^2 = 51/(51 \text{ d.o.f.})$ (47 % CL) for $\nu_\mu \rightarrow \nu_s$ with $\Delta m^2 < 0$ and $\chi_{min}^2 = 50/(51 \text{ d.o.f.})$ (51 % CL) for $\nu_\mu \rightarrow \nu_s$ with $\Delta m^2 > 0$. We thus conclude that the quality of the global description of the atmospheric neutrino data in terms of neutrino oscillation is better for the $\nu_\mu \rightarrow \nu_\tau$ channel, although oscillations into $\nu_\mu \rightarrow \nu_s$ cannot be statistically ruled out, on the basis of the global fit to the full set of observables.

We have also presented a sample of predicted zenith-angle distributions for the best-fit points corresponding to the various oscillation channels. Specifically, we showed the angular distribution corresponding to the four Super-Kamiokande data sets (sub-GeV, multi-GeV, stopping muons and through-going muons) and the angular distributions for upgoing muons at MACRO and Baksan. By using the zenith-angle distribution expected for contained events and up-going muon data at Super-Kamiokande in the presence of oscillations, we have compared the relative goodness of the three possible oscillation channels. This allowed one to understand why the $\nu_\mu \rightarrow \nu_\tau$ channel gives a better description than the $\nu_\mu \rightarrow \nu_s$ cases. On the one hand, due to matter effects, one finds that for the sterile case the up-down asymmetry in the multi-GeV sample is slightly smaller than observed. Moreover, also due to matter effects, the upgoing-muon distributions in the case of $\nu_\mu \rightarrow \nu_s$ are flatter than for $\nu_\mu \rightarrow \nu_\tau$, while the data show a slightly steeper angular dependence which can be better described by $\nu_\mu \rightarrow \nu_\tau$.

To conclude, we compare our determinations of the allowed neutrino oscillation parameters from the analyses of the atmospheric neutrino data with the expected sensitivities of future long-baseline experiments such as K2K [32] and MINOS [33] (Fig. 7). We notice that, for the oscillations $\nu_\mu \rightarrow \nu_\tau$, K2K can cover most of the 90% CL allowed region while the MINOS test of NC/CC is sensitive to the complete 99% CL region of oscillation parameters. For oscillations into sterile neutrinos, a situation where only a CC disappearance test can be performed at long baseline experiments, K2K can cover a portion of the region allowed at 90% CL, while the full 99% CL allowed regions are completely accessible to the MINOS experiment.

APPENDIX: STATISTICAL ANALYSIS

In this Appendix, we discuss the errors and correlations employed in our analysis.

A. Errors

Data errors contain the experimental statistical and systematic errors as well as the uncertainties arising from event mis-identification, as quoted by the experimental Collaborations. In the theoretical calculations of event rates and upgoing muon fluxes, we take into account the uncertainty in the atmospheric neutrino flux and the uncertainties in the charged-current neutrino cross-sections [27]. We also include, the Monte Carlo (MC) statistical errors estimated by the experimental Collaborations with the simulations of their detectors. This uncertainty depends on the number of simulated Monte-Carlo events.

The flux uncertainty is taken to be 30% at lower energies, relevant for contained events, and 20% at higher energies, characteristic of upward going muons. Nuclear cross-section uncertainties are taken to be 10% for all the contained event samples, except for Soudan2 for which we used the values 7.5% and 6.4% for e -like and μ -like events, respectively [5]. For stopping and through-going muons, as cross-section uncertainties we use 11.4% and 14.1%, respectively [9]. The Monte–Carlo statistical errors are estimated from the simulated exposure, as given by the experimental Collaborations, under the assumption that the e - and μ -like contained events follow a binomial distribution.

B. Correlations

There is a large number of correlations, both from experimental and from theoretical sources. In our analysis, data errors between different experiments are assumed to be uncorrelated, *i.e.*

$$\begin{aligned}\rho_{\alpha\alpha}^{DATA}(A, A) &= 1 \quad (\alpha = e, \mu) \quad \text{for all data samples} \\ \rho_{\alpha\beta}^{DATA}(A, B) &= 0 \quad (\alpha, \beta = e, \mu) \quad \text{if } A \neq B,\end{aligned}\tag{16}$$

while the correlations in the theoretical quantities referring to different experiments (*i.e.*, for $A \neq B$) are assumed to arise from the correlations amongst the theoretical errors for the neutrino flux normalization and amongst the theoretical uncertainties of the neutrino interaction cross section.

In order to determine the different entries, we have classified the experiments in four samples:

- *sub-GeV* (SG): Frejus, IMB, Nussex, Soudan2, Kam sub-GeV and Super–Kam sub-GeV
- *multi-GeV* (MG): Kam multi-GeV and Super–Kam multi-GeV
- *stopping muons* (STOP): Super–Kam
- *thru-going muons* (THRU): Super–Kam, MACRO and Soudan.

We then estimate the correlations as follows,

$$\rho_{\alpha\beta}^{TH}(A, B) = \rho_{\alpha\beta}^{flux}(A, B) \times \frac{\sigma_{\alpha}^{flux}(A)\sigma_{\beta}^{flux}(B)}{\sigma_{\alpha}^{TH}(A)\sigma_{\beta}^{TH}(B)} + \rho_{\alpha\beta}^{cross}(A, B) \times \frac{\sigma_{\alpha}^{cross}(A)\sigma_{\beta}^{cross}(B)}{\sigma_{\alpha}^{TH}(A)\sigma_{\beta}^{TH}(B)}$$

where the correlation $\rho_{\alpha\beta}^{flux}$ and $\rho_{\alpha\beta}^{cross}$ can be computed from the allowed uncertainties on the corresponding ratios by means of:

$$\begin{aligned}\sigma_{Rf}^2(A : \alpha, B : \beta) &\equiv \sigma^2\left(\frac{\Phi_{\alpha}(A)}{\Phi_{\beta}(B)}\right) = \sigma_{\alpha}^2{}^{flux}(A) + \sigma_{\beta}^2{}^{flux}(B) - 2\rho_{\alpha\beta}^{flux}(A, B)\sigma_{\alpha}^{flux}(A)\sigma_{\beta}^{flux}(B) \\ \sigma_{Rc}^2(A : \alpha, B : \beta) &\equiv \sigma^2\left(\frac{\sigma_{\alpha}^{CC}(A)}{\sigma_{\beta}^{CC}(B)}\right) = \sigma_{\alpha}^2{}^{cross}(A) + \sigma_{\beta}^2{}^{cross}(B) - 2\rho_{\alpha\beta}^{cross}(A, B)\sigma_{\alpha}^{cross}(A)\sigma_{\beta}^{cross}(B)\end{aligned}$$

We assume that the errors in the above defined ratios of the neutrino fluxes and the neutrino cross-sections between the different experiments arise from three sources: the flavour dependence, the energy dependence and the angular dependence [28].

$$\begin{aligned}\sigma_{Rf}^2(A : \alpha, B : \beta) &= \sigma_{Rf,flav}^2(A : \alpha, B : \beta) + \sigma_{Rf,en}^2(A : \alpha, B : \beta) + \sigma_{ang}^2(A : \alpha, B : \beta) \\ \sigma_{Rc}^2(A : \alpha, B : \beta) &= \sigma_{Rc,flav}^2(A : \alpha, B : \beta) + \sigma_{Rc,en}^2(A : \alpha, B : \beta) + \sigma_{ang}^2(A : \alpha, B : \beta)\end{aligned}$$

For sub-GeV data samples, there are additional sources of uncertainties with respect to the other data sets. For instance, the form of the geo-magnetic cut-off used in the neutrino flux, the nuclear modeling for the neutrino interaction cross section, the neutrino production in the atmosphere. These additional uncertainties allow a large variation of the expectations for sub-GeV experiments, without affecting the predictions for higher energy events. Thus we neglect the correlations in the theoretical errors between sub-GeV events and any of the higher energy samples. Moreover the different experimental collaborations use different calculations for the neutrino interaction cross section, thus we neglect correlations between the theoretical errors of the interaction cross sections for different detectors. For all other cases we use the following values:

$\sigma_{Rf,flav}^2(A : \alpha, B : \beta) = 0$	for $\alpha = \beta$
$\sigma_{Rf,flav}^2(A : e, B : \mu) = 5\%$	for A, B unbinned (SG)
$\sigma_{Rf,flav}^2(A : e, B : \mu) = 10\%$	for A, B binned (SG) or (MG)
$\sigma_{Rf,flav}^2(A : \mu, B : \mu) = 10\%$	for A in (MG) and B in (STOP)
$\sigma_{Rf,flav}^2(A : \mu, B : \mu) = 14\%$	for A in (MG) and B in (THRU)
$\sigma_{Rf,en}^2(A : \alpha, B : \beta) = 0$	for A, B in the same sample
$\sigma_{Rf,en}^2(A : \mu, B : \mu) = 5\%$	for A in (MG) and B in (STOP)
$\sigma_{Rf,en}^2(A : \mu, B : \mu) = 10\%$	for A in (STOP) and B in (THRU)
$\sigma_{Rf,en}^2(A : \mu, B : \mu) = 11\%$	for A in (MG) and B in (THRU)
$\sigma_{Rc,flav}^2(A : \alpha, B : \beta) = 0$	for $\alpha = \beta$
$\sigma_{Rc,flav}^2(A : e, B : \mu) = 3 \text{ to } 10\%$	for A, B (SG)
$\sigma_{Rc,fl}^2(A : e, B : \mu) = 2 \text{ to } 4\%$	for A, B in (MG)
$\sigma_{Rc,en}^2(A : \alpha, B : \beta) = 0$	for A, B in the same sample
$\sigma_{Rc,en}^2(A : \alpha, B : \mu) = 5\%$	for A in (MG) and B in (STOP)
$\sigma_{Rc,en}^2(A : \alpha, B : \mu) = 7\%$	for A in (MG) and B in (THRU)
$\sigma_{Rc,en}^2(A : \mu, B : \mu) = 5\%$	for A in (STOP) and B in (THRU)
$\sigma_{ang}^2(A : \alpha, B : \beta) = 5\% \cos(\theta_A) - \cos(\theta_B) $	for all angular distributions

With this we get that the smallest non-vanishing theoretical correlation within the Super-Kamiokande samples occurs between the theoretical errors for most vertical multi-GeV electron bin and the most horizontal thru-going muon bin and it takes the value $\rho^{TH} = 0.735$ while, for example, the correlation between the theoretical errors of the two most horizontal bins of the thru-going muon sample is $\rho^{TH} = 0.989$.

ACKNOWLEDGMENTS

We thank Ricardo Vazquez for providing us with the codes for the evaluation of the muon energy loss, and Todor Stanev who provided us with his atmospheric neutrino fluxes. It is a pleasure also to thank Mark Messier, Teresa Montaruli and Olga Suvorova for useful discussions. This work was supported by DGICYT under grants PB98-0693 and PB97-1261, and by the TMR network grant ERBFMRXCT960090 of the European Union.

REFERENCES

- [1] J. Bahcall and R. Davis, “The evolution of neutrino astronomy,” astro-ph/9911486; recent theoretical updates of data are given by M. C. Gonzalez-Garcia, P. C. de Holanda, C. Pena-Garay and J. W. F. Valle, hep-ph/9906469 (for MSW) and by V. Barger and K. Whisnant, Phys. Rev. **D59**, 093007 (1999) and by S. Goswami, D. Majumdar and A. Raychaudhuri, hep-ph/9909453 (vacuum oscillation case).
- [2] K. Daum *et al.* Z. Phys. **C66**, 417 (1995).
- [3] M. Aglietta *et al.*, Europhys. Lett. **8**, 611 (1989).
- [4] R. Becker-Szendy *et al.*, Phys. Rev. **D46**, 3720 (1992).
- [5] W. W. M. Allison *et al.*, Phys. Lett. **B449**, 137 (1999).
- [6] T. Kafka, hep-ex/9912060, Proc. of the *Sixth International Workshop on Topics in Astroparticle and Underground Physics*, TAUP99, Paris September 1999.
- [7] H. S. Hirata *et al.*, Phys. Lett. **B280**, 146 (1992); Y. Fukuda *et al.*, *ibid* **B335**, 237 (1994).
- [8] Y. Fukuda *et al.*, Phys. Lett. **B433**, 9 (1998); Phys. Lett. **B436**, 33 (1998).
- [9] Y. Fukuda *et al.*, Phys. Lett. **B467**, 185 (1999); Phys. Rev. Lett. **82**, 2644 (1999).
- [10] M. Nakahata, Proc. of the *Sixth International Workshop on Topics in Astroparticle and Underground Physics*, TAUP99, Paris September 1999; SuperKamiokande Collaboration (A. Habig for the collaboration). Talk given at American Physical Society (APS) Meeting of the Division of Particles and Fields (DPF 99), Los Angeles, CA, 5-9 Jan 1999.
- [11] F. Ronga [MACRO Collaboration], hep-ex/0001058, Proc. of the *Sixth International Workshop on Topics in Astroparticle and Underground Physics*, TAUP99, Paris September 1999.
- [12] M. M. Boliev, A. V. Butkevich, A. E. Chudakov, S. P. Mikheev, O. V. Suvorova and V. N. Zakidyshev, Nucl. Phys. Proc. Suppl. **70**, 371 (1999).
- [13] G. Barr, T. K. Gaisser and T. Stanev, Phys. Rev. **D 39** (1989) 3532 and Phys. Rev. **D38**, 85.
- [14] V. Agrawal *et al.*, Phys. Rev. **D53**, 1314 (1996); M. Honda, T. Kajita, S. Midorikawa and K. Kasahara, Phys. Rev. **D52**, 4985 (1995).
- [15] N. Fornengo, M. C. Gonzalez-Garcia and J. W. F. Valle, hep-ph/9906539; M. C. Gonzalez-Garcia *et al.*, Phys. Rev. Lett. **82**, 3202 (1999) [hep-ph/9809531]; M. C. Gonzalez-Garcia, hep-ph/9808203; V. Barger, J. G. Learned, P. Lipari, M. Lusignoli, S. Pakvasa and T. J. Weiler, Phys. Lett. **B462**, 109 (1999) [hep-ph/9907421]; V. Barger, J. G. Learned, S. Pakvasa and T. J. Weiler, Phys. Rev. Lett. **82**, 2640 (1999)
- [16] M. Gasperini, Phys. Rev. **D38**, 2635 (1988); J. Pantaleone, A. Halprin, C.N. Leung, Phys. Rev. **D47**, 4199 (1993); A. Halprin, C.N. Leung, J. Pantaleone Phys. Rev. **D53**, 5365 (1996); S. Coleman, S. L. Glashow, Phys. Lett. **B405**, 249 (1997); S. L. Glashow, A. Halprin, P.I. Krastev, C.N. Leung, J. Pantaleone, Phys. Rev. **D56**, 2433 (1997). S. Coleman, S. L. Glashow, Phys. Rev. **D59**, 116008 (1999). G.L. Fogli, E. Lisi, A. Marrone, G. Scioscia, Phys. Rev. **D59**, 117303 (1999); *ibid* **D60**, 053006 (1999).
- [17] M. C. Gonzalez-Garcia, H. Nunokawa, O. L. G. Peres, T. Stanev and J. W. F. Valle, Phys. Rev. **D58**, 033004 (1998); M.C. Gonzalez-Garcia, H. Nunokawa, O.L. Peres and J. W. F. Valle, Nucl. Phys. **B543**, 3 (1999).
- [18] R. Foot, R. R. Volkas and O. Yasuda, Phys. Rev. **D58**, 013006 (1998); O. Yasuda, Phys. Rev. **D58**, 091301 (1998); G. L. Fogli, E.Kh. Akhmedov, A.Dighe, P. Lipari and A.Yu. Smirnov, hep-ph/9808270.

- [19] Y. Fukuda *et al.*, Phys. Rev. Lett. **81**, 1562 (1998).
- [20] T. K. Gaisser and T. Stanev, Phys. Rev. **D57** 1977 (1998).
- [21] W. Lohmann, R. Kopp and R. Voss, CERN Yellow Report EP/85-03.
- [22] E. Zas, F. Halzen, R.A. Vazquez, Astropart. Phys. **1** 297 (1993).
- [23] P. Lipari, M. Lusignoli Phys. Rev. **D58**, 073005 (1998).
- [24] E. Lisi and D. Montanino, Phys. Rev. **D56**, 1792 (1997).
- [25] A.M. Dziewonski and D.L. Anderson, Phys. Earth Planet. Inter. **25**, 297 (1981).
- [26] CHOOZ Collaboration, M. Apollonio *et al.*, Phys. Lett. B **420** 397(1998).
- [27] G. L. Fogli, E. Lisi, Phys. Rev. **D52**, 2775 (1995); G. L. Fogli, E. Lisi and D. Montanino, Phys. Rev. **D49**, 3626 (1994); Astrop. Phys. **4**, 177 (1995); G. L. Fogli, E. Lisi, D. Montanino and G. Scioscia Phys. Rev. **D55**, 485 (1997).
- [28] E. Lisi, A. Marrone, G. Scioscia, Phys. Rev. **D59**, 033001 (1999).
- [29] T. K. Gaisser, M. Honda, K. Kasahara, H. Lee, S. Midorikawa, V. Naumov and T. Stanev; Phys. Rev. **D54**, 5578 (1996).
- [30] P. Lipari, M. Lusignoli Phys. Rev. **D60**, 013003 (1999).
- [31] A. De Rujula, P. Hernandez, hep-ph/0001124
- [32] KEK-SK Collaboration, C. Yanagisawa, proceedings of International Workshop on Physics Beyond The Standard Model: from Theory to Experiment, Valencia, Spain, October 13-17, 1997, ed. by I. Antoniadis, L. Ibanez and J. W. F. Valle (World Scientific, 1998); KEK-SK Collaboration, *Proposal for Participation in Long-Baseline Neutrino Oscillation Experiment E362 at KEK*, W. Gajewski *et al.* (unpublished).
- [33] MINOS Collaboration, D. Michael *et al.*, Proceedings of *XVI International Workshop on Weak Interactions and Neutrinos*, Capri, Italy, 1997, edited by G. Fiorilo *et al.*, [Nucl. Phys. B (Proc. Suppl.)**66** (1998) 432].

TABLES

Data sets	χ_{SM}^2	$\sin^2(2\theta)$			Δm^2 (10^{-3} eV 2)			χ_{\min}^2			d.o.f.
		ν_τ	ν_s (-)	ν_s (+)	ν_τ	ν_s (-)	ν_s (+)	ν_τ	ν_s (-)	ν_s (+)	
FISN	27	0.97	0.99	1.00	3.0	2.6	2.8	13	13	13	6
Kamioka sub-GeV	16	0.82	0.86	0.95	400	12	7.0	0.02	0.02	0.02	0
Kamioka multi-GeV	19	0.95	0.95	0.93	23	25	25	6.8	6.8	6.7	8
<i>Kamioka combined</i>	35	0.85	0.86	0.86	25	22	21	7.3	7.2	7.0	10
SK sub-GeV	27	1.0	1.0	1.0	1.3	1.3	1.3	2.4	2.7	2.7	8
SK multi-GeV	42	0.98	1.0	0.99	1.7	3.5	3.5	6.3	9.0	8.9	8
<i>SK contained</i>	69	1.0	1.0	0.98	1.7	2.7	2.6	8.9	13	13	18
SK stop μ	8.4	1.0	1.0	0.93	3.0	3.5	3.5	1.3	2.4	2.3	3
SK thru μ	19	0.78	1.0	0.53	11	8.1	21	10	13	10	8
<i>SK upgoing</i>	30	0.94	1.0	0.86	3.5	4.0	5.3	13	16	15	13
<i>SK combined</i>	122	0.98	1.0	0.93	2.6	3.5	3.5	24	33	32	33
MACRO thru μ	27	1.0	1.0	0.07	2.0	8.1	12	16	24	23	8
MACRO thru μ	27			1.0			7.9			24	8
Baksan thru μ	22	0.41	0.66	0.73	6.1	2.0	3.0	21	19	17	8
<i>Contained comb</i>	103	0.99	1.0	0.97	1.7	2.7	2.6	37	40	40	38
<i>Upgoing μ comb</i>	76	0.99	1.0	0.97	3.0	3.0	4.6	56	60	59	33
Global	214	0.92	1.0	0.85	2.6	3.0	4.0	74	90	86	73
Global*	182	1.0	1.0	0.95	3.0	3.0	4.0	58	76	75	61
Global**	156	0.99	1.0	0.96	3.0	4.0	4.0	41	51	50	51

TABLE I. Minimum χ^2 values and best-fit points for the various data sets and oscillation channels. For the $\nu_\mu \rightarrow \nu_s$ channels, we have denoted by (-) the case with $\Delta m^2 < 0$ and by (+) the case with $\Delta m^2 > 0$. **Global** refers to the best-fit for the global analysis which includes all the data sets listed above. **Global*** includes all the data sets, except for Frejus, Nussex and Baksan. **Global**** includes all the data sets, except for Frejus, Nussex, Baksan and MACRO. For the sake of comparison we also list the χ_{SM}^2 expected in the absence of oscillations. Notice that for the MACRO data set, for the $\nu_\mu \rightarrow \nu_s$ channel ($\Delta m^2 > 0$) we find two almost degenerate minima.

FIGURES

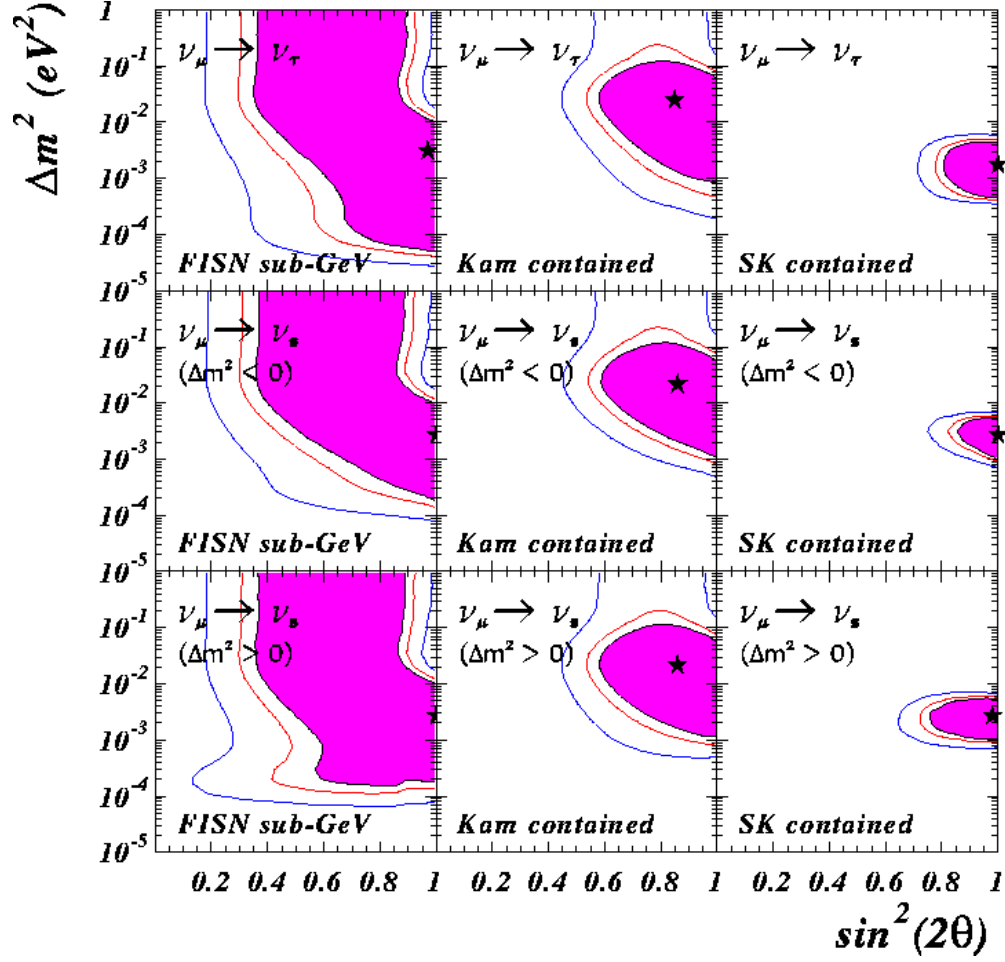


FIG. 1. Allowed regions in the $\sin^2(2\theta) - \Delta m^2$ parameter space for different combinations of contained events and for the different oscillation channels. The shaded areas refer to the 90% CL, while the inner (outer) lines stand for 95% (99%) CL, respectively. FISN labels the combined rates from Frejus, IMB, Soudan2 and Nussex experiments. For each panel, the best fit point is marked with a star.

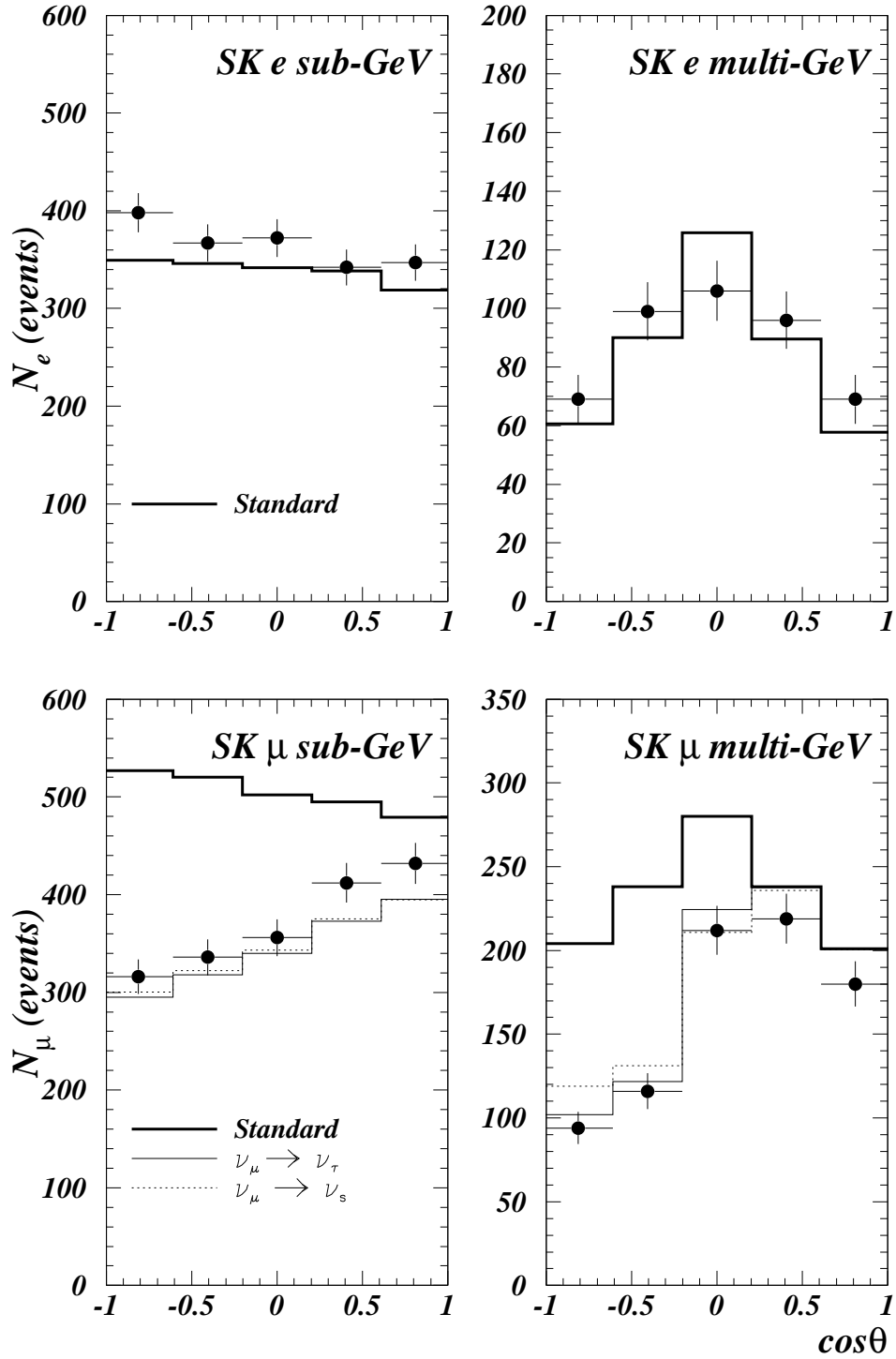


FIG. 2. Zenith-angle distributions for the Super-Kamiokande electron-like and muon-like sub-GeV and multi-GeV events, together with our prediction in the absence of oscillation (thick solid line) and the predictions for the best fit points for each data set in the different oscillation channels: $\nu_\mu \rightarrow \nu_\tau$ (thin solid line) and $\nu_\mu \rightarrow \nu_s$ (dotted line). Since the best-fit point occurs for maximal mixing, the histograms for $\nu_\mu \rightarrow \nu_s$ are independent of the Δm^2 sign. The errors displayed in the experimental points are statistical.

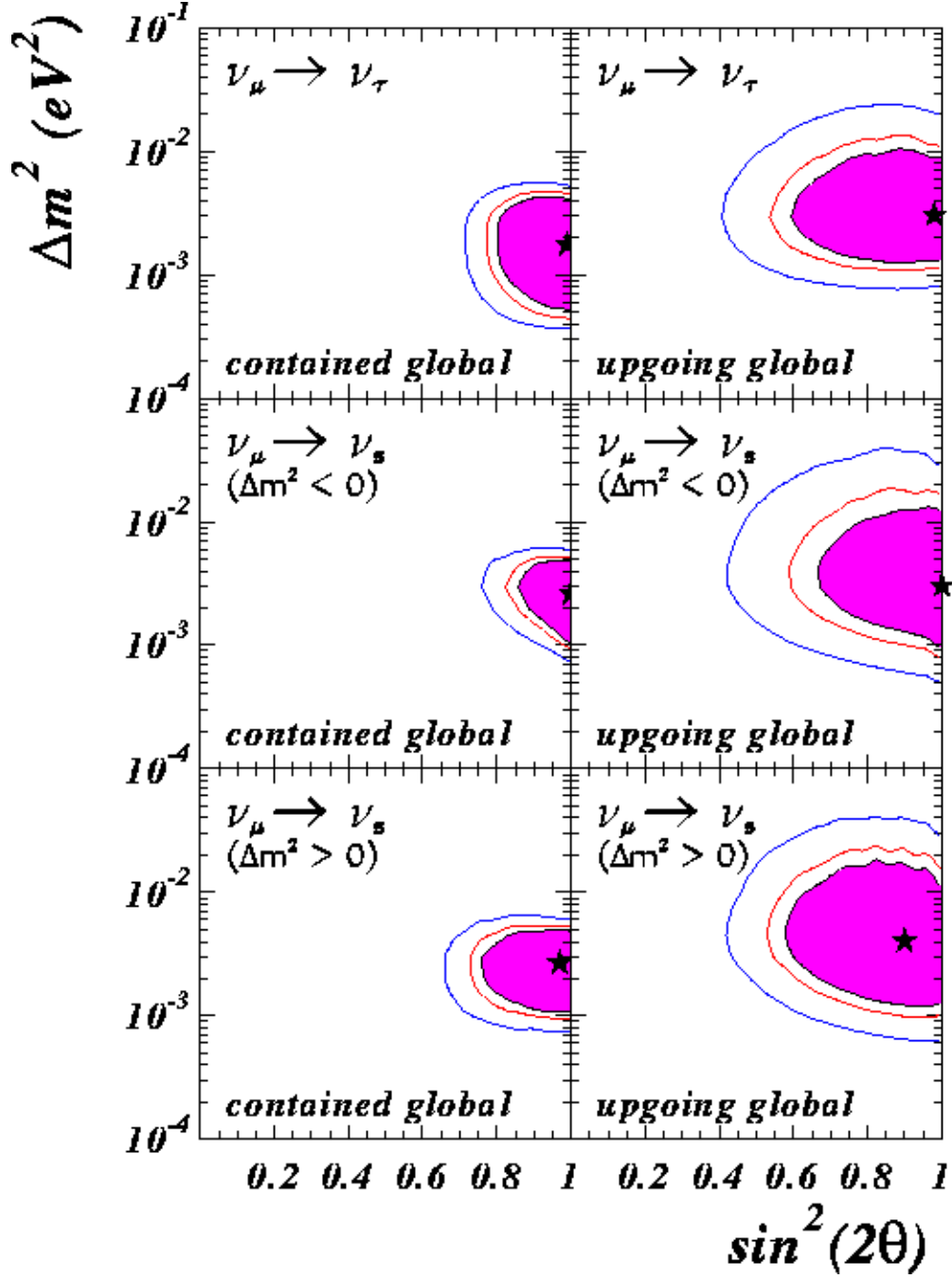


FIG. 3. Allowed regions in the $\sin^2(2\theta) - \Delta m^2$ parameter space for the combination of all contained event data (left panels) and the combination of the upgoing muon data (right panels). Notations are as in Fig. 1.

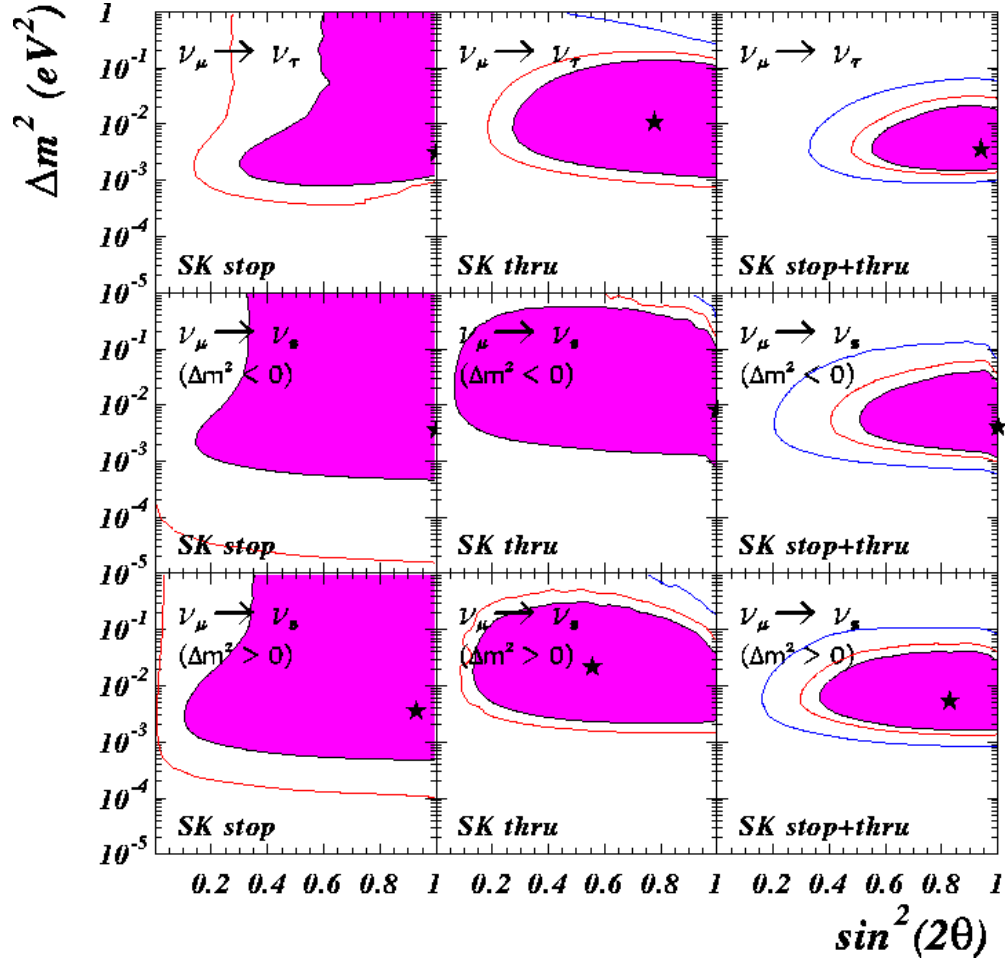


FIG. 4. Allowed regions in the $\sin^2(2\theta) - \Delta m^2$ parameter space for the Super-Kamiokande data on upgoing muons. Notations are as in Fig. 1.

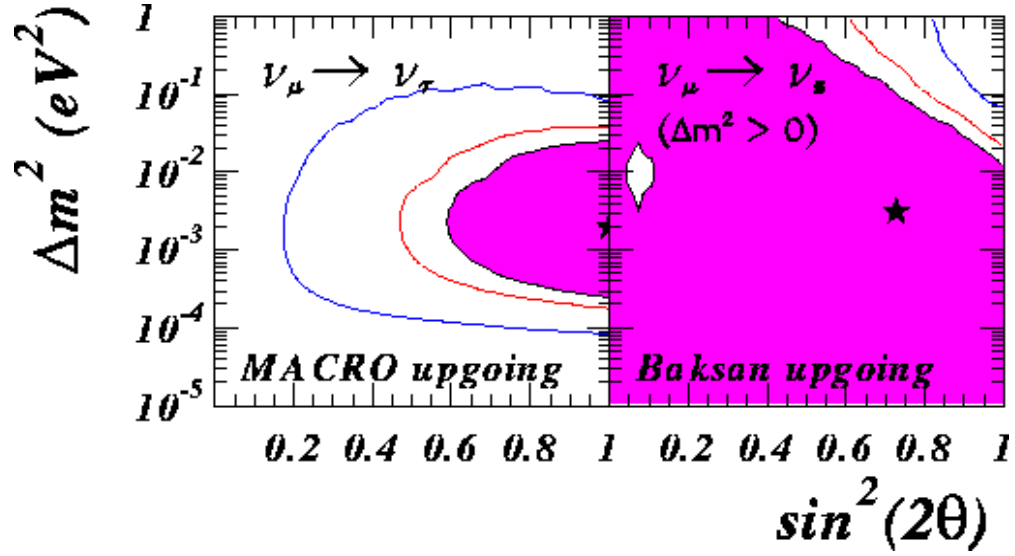


FIG. 5. Allowed regions in the $\sin^2(2\theta) - \Delta m^2$ parameter space for the MACRO and Baksan data. The cases which provide the best agreement with the data are presented: $\nu_\mu \rightarrow \nu_\tau$ for MACRO and $\nu_\mu \rightarrow \nu_s$ with $\Delta m^2 > 0$ for Baksan. Notations are as in Fig. 1.

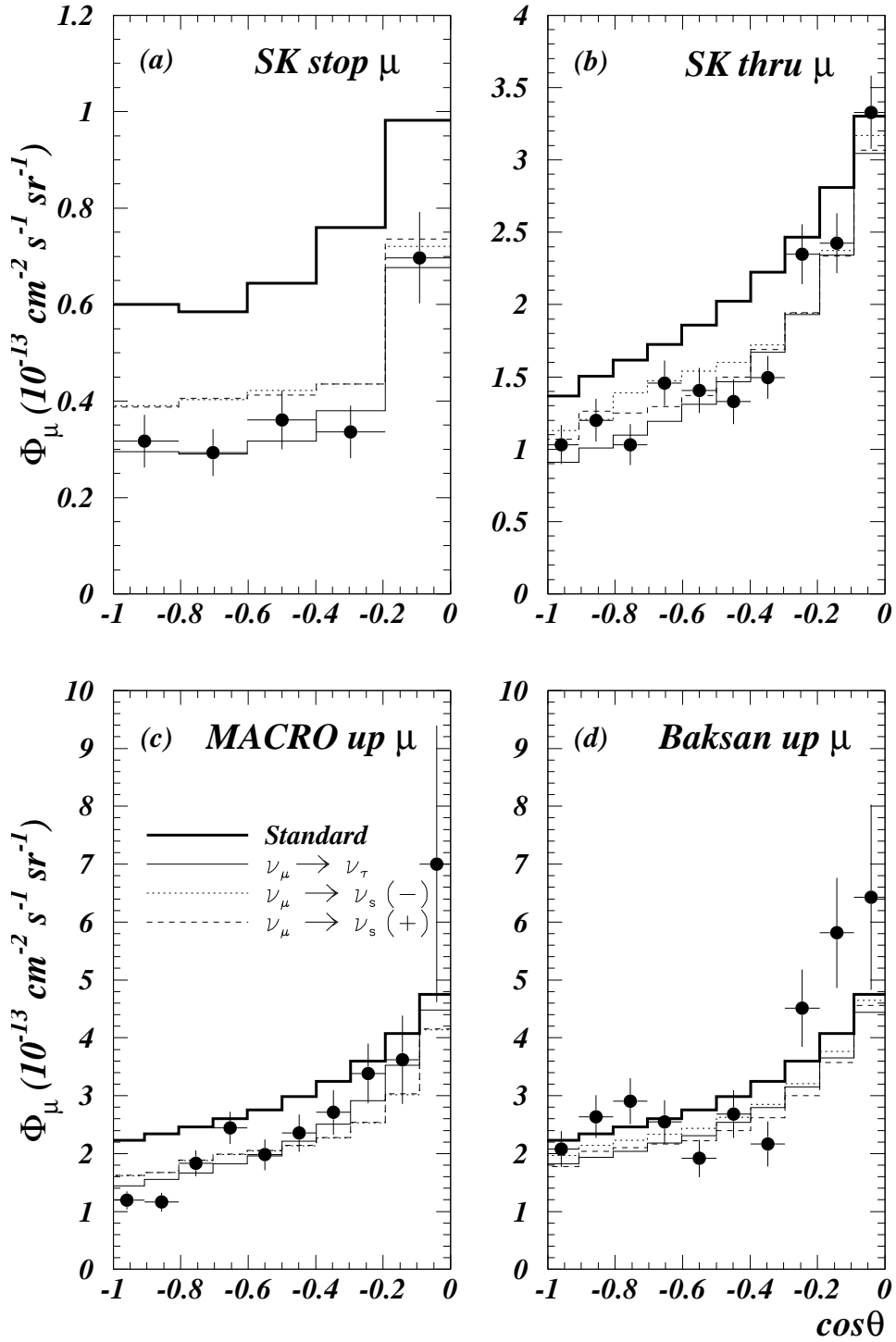


FIG. 6. Zenith-angle distributions for upward-going muon events in Super-Kamiokande, MACRO and Baksan, together with our prediction in the absence of oscillation (thick solid line) as well as the predictions for the best fit points for each data set. The different lines refer to: $\nu_\mu \rightarrow \nu_\tau$ (thin solid line), $\nu_\mu \rightarrow \nu_s$ with $\Delta m^2 < 0$ (dotted line), and $\nu_\mu \rightarrow \nu_s$ with $\Delta m^2 > 0$ (dashed line). The errors displayed in the experimental points are statistical.

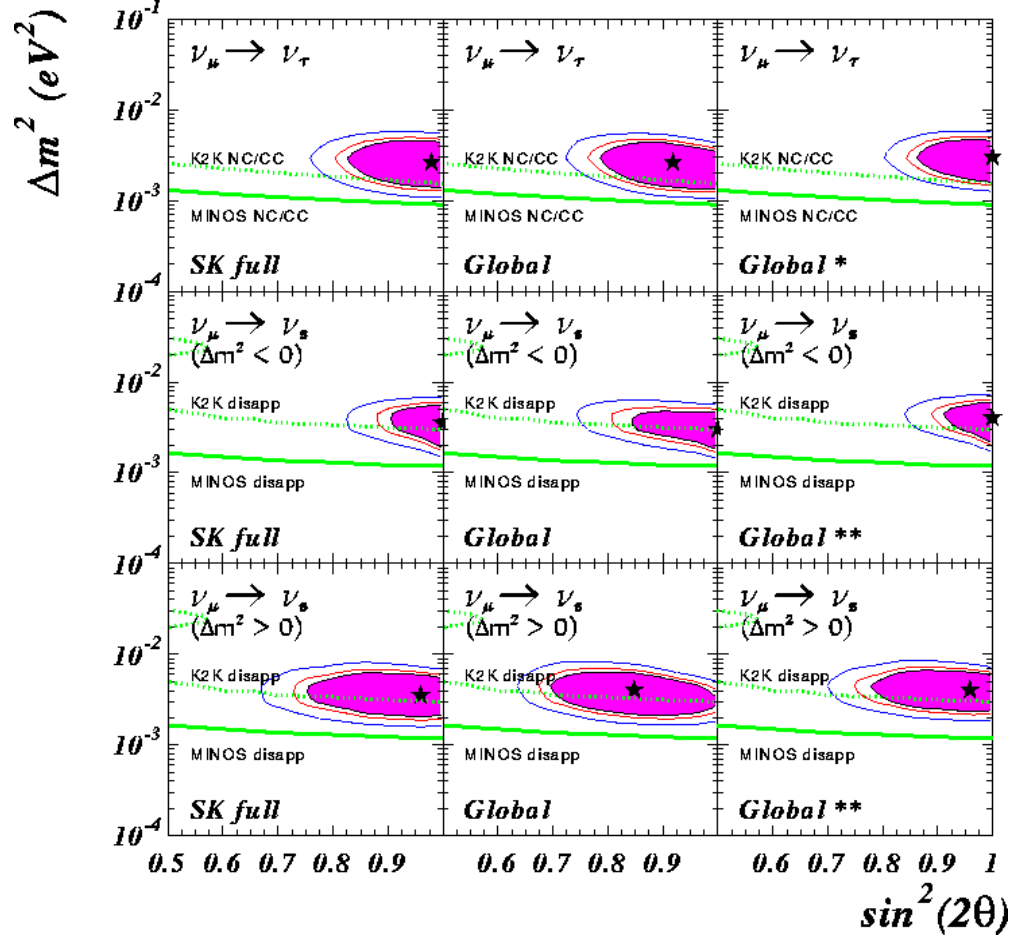


FIG. 7. Allowed regions in the $\sin^2(2\theta) - \Delta m^2$ parameter space for the full combination of Super-Kamiokande event data (left panels), the full data sample from all atmospheric neutrino experiments (central panels) and the combination of *positive result* atmospheric neutrino experiments (right panels). The shaded areas refer to the 90% CL, while the inner (outer) lines stand for 95% (99%) CL, respectively and the best fit points are indicated by a star. With Global* we indicate that all the data sets are included, except for Frejus, Nussex and Baksan. Global** includes all the data sets, except for Frejus, Nussex, Baksan and MACRO. Expected sensitivities of the future long-baseline experiments K2K and MINOS are also displayed for each oscillation channel.

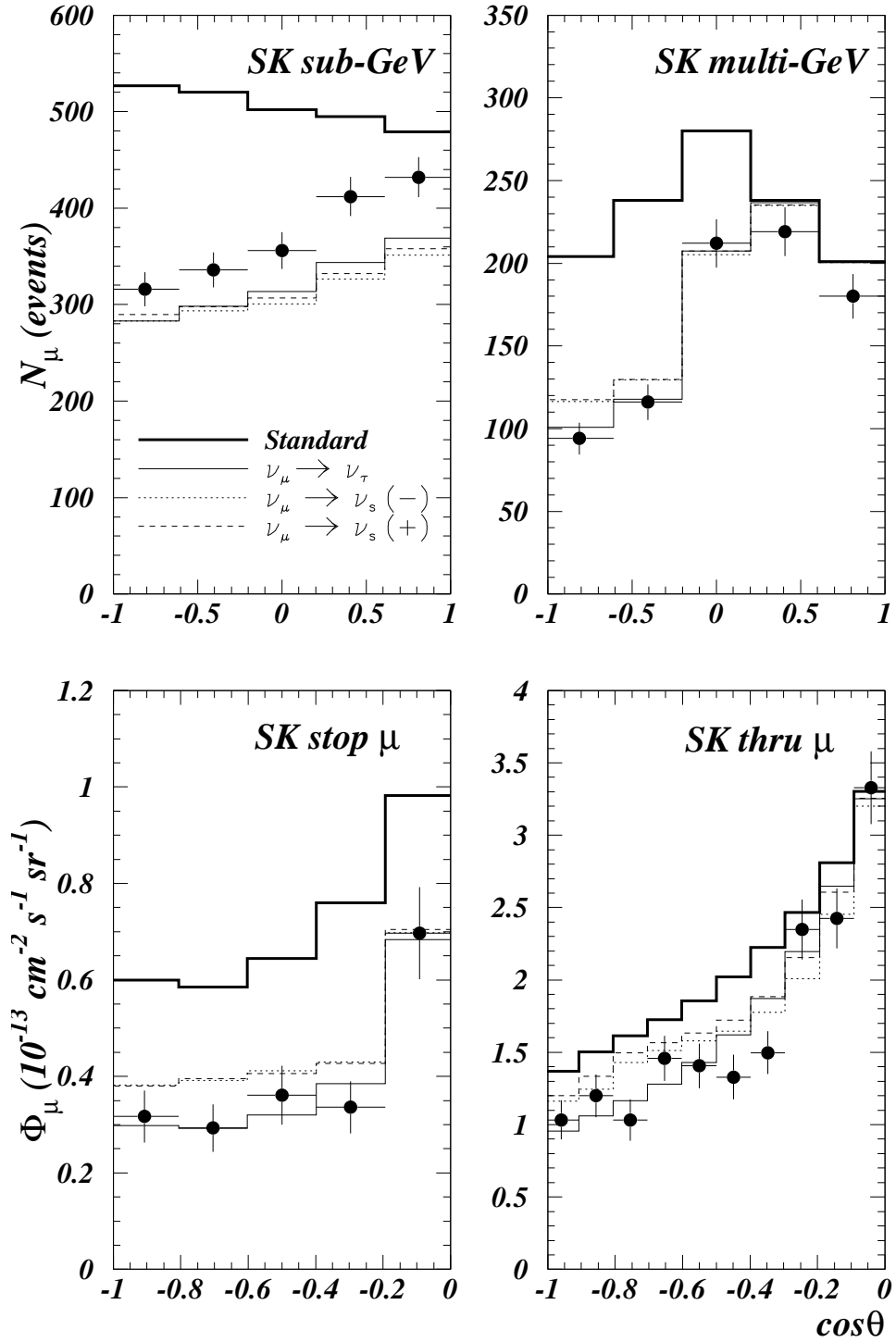


FIG. 8. Zenith-angle distributions for the Super-Kamiokande data sets, together with our prediction in the absence of oscillation (thick solid line) as well as the predictions for the best fit points obtained in the global analysis of the data (denoted as Global** in Table I). The different lines refer to the various oscillation channels: $\nu_\mu \rightarrow \nu_\tau$ (thin solid line), $\nu_\mu \rightarrow \nu_s$ with $\Delta m^2 < 0$ (dotted line), and $\nu_\mu \rightarrow \nu_s$ with $\Delta m^2 > 0$ (dashed line). The errors displayed in the experimental points are statistical.